metals

MDPI

Article

Characterisation of a Real-World Søderberg Electrode

Ralph Ivor Glastonbury [1], Johan Paul Beukes [1,*], Pieter Gideon van Zyl [1], Merete Tangstad [2], Eli Ringdalen [3], Douglas Dall [4], Joalet Dalene Steenkamp [5,6] and Masana Mushwana [5]

1 Chemical Resource Beneficiation, North-West University, Potchefstroom 2520, South Africa; 23032898@student.g.nwu.ac.za (R.I.G.); Pieter.VanZyl@nwu.ac.za (P.G.v.Z.)
2 Department of Materials Science and Engineering, Norwegian University of Science and Technology (NTNU), 7465 Trondheim, Norway; merete.tangstad@ntnu.no
3 Metal Production and Processing, Department of Materials and Chemistry, Sintef, 7465 Trondheim, Norway; Eli.Ringdalen@sintef.no
4 Glencore Alloys, Rustenburg 0300, South Africa; Douglas.Dall@glencore.co.za
5 Pyrometallurgy Division, Mintek, Randburg 2125, South Africa; JoaletS@mintek.co.za (J.D.S.); MasanaM@mintek.co.za (M.M.)
6 Faculty of Engineering & the Built Environment, School of Chemical & Metallurgical Engineering, University of the Witwatersrand, Johannesburg 2000, South Africa
* Correspondence: paul.beukes@nwu.ac.za; Tel.: +27-18-299-2337

Abstract: Very little research on Søderberg electrodes has been published in the journal peer reviewed public domain. The main aim of this work is to characterise a Søderberg electrode that was cut off approximately 0.5 m below the contacts shoes of a submerged arc furnace. Additionally, the characterisation data can be used to verify if Søderberg electrode models accurately predict important electrode characteristics. The operational history (slipping, current, and paste levels) proved that the case study electrode was a representative specimen. The characterisation results indicated no significant electrical resistivity, degree of graphitisation (DOG), and bulk density changes from 0.7 to 2.7 m on the non-delta side (outward facing), while these characteristics changed relatively significantly on the delta side (inward facing) of the electrode. The area where the submerged arc would mostly like jump off the electrode had the lowest resistivity, as well as highest DOG and bulk density. No significant difference in porosity as a function of length below the contact shoes were observed; however, slight increases occurred near the perimeters. It was postulated that oxidation of carbon resulted in increased pore volumes near the electrode perimeter. No significant difference in compressive breaking strength was observed over the electrode area investigated.

Keywords: Søderberg electrodes; submerged arc furnace (SAF); ferro-alloy production; ferrochrome; electrical resistivity; degree of graphitisation; bulk density; porosity; compressive breaking strength

Citation: Glastonbury, R.I.; Beukes, J.P.; van Zyl, P.G.; Tangstad, M.; Ringdalen, E.; Dall, D.; Steenkamp, J.D.; Mushwana, M. Characterisation of a Real-World Søderberg Electrode. *Metals* **2021**, *11*, 5. https://dx.doi.org/10.3390/met11010005

Received: 31 October 2020
Accepted: 18 December 2020
Published: 22 December 2020

1. Introduction

Since its development in the early 1900s [1], Søderberg electrodes have been used extensively in submerged arc furnaces (SAFs) to conduct electrical current from a transformer(s) to the smelting zone [2]. Various authors have presented representations of a Søderberg electrode column and/or described the processes associated with it, e.g., [2–10]. Such a column typically consists of a cylindrical steel casing that extends from a building level well above the furnace, down into the smelting zone. The casing serves as the mould for the electrode paste, which contains a binder (e.g., coal tar pitch) mixed with a solid aggregate (e.g., calcined anthracite or coke), to form the electrode during operation. The casing also has longitudinal fins, which add dimensional stability to the casing and the unbaked electrode. Resistive heating of current passing through the casing, fins, and paste, as well as heat conducted upward from the SAF in the electrode column melt the electrode paste at temperatures above its softening point to fill the casing. Electrode paste softening temperatures have been reported to be in the range of 65 to 134 °C [11]. Solid electrode paste

is added at regular intervals via the top of the electrode casing to maintain a steady level of solid (un-melted) and liquid paste (that have filled the casing). The casing is slipped (lowered in relation to clamping devices that hold the electrode) relatively small distances on a shift basis (usually 8 h long), and longer slips are taken if an electrode break occurs, or if the electrode is shorter than ideal. All the afore-mentioned result in the melted paste being exposed to increasing temperatures as it approaches the so-called contact shoes. Contact shoes are large copper (or copper alloy) components that are pressed against the casing to conduct electrical current into the electrode. Before the liquid electrode paste reaches the bottom of the contact shoes, it should ideally be transformed into solid carbonaceous material. The temperature at which the paste transforms from a liquid to a solid is termed the baking isotherm. This transformation temperature has been reported to be between 450 and 475 °C [11]. As the carbonaceous electrode descends further into the SAF temperatures increase, which results in further baking.

Good Søderberg electrode management, together with other aspects such as maintaining a suitable metallurgical balance (to obtain product within specifications and the correct slag chemistry), high electrical power input (assuming fixed specific energy consumption, production volume is directly related to power input), and feeding the furnace appropriately (without feed it cannot produce and asymmetrical feed could lead to damage) form the basis for safe (occupational health and safety of workers), environmentally responsible (limiting emissions), and profitable smelting operations. However, good Søderberg electrode management implies that a multitude of actions and tracking of parameters need to take place on a shift and daily basis.

Very harsh conditions in the SAFs lead to severe mechanical and thermal stresses, which result in unavoidable wear of the electrode tips. Furthermore, thermal stresses associated with shutdowns and operational instability may cause anything from inconsequential hard electrode breaks to disastrous green breaks [7,8]. Broken electrodes can negatively impact process productivity (e.g., lower electrical power input, damage to equipment, or even prolonged shutdowns to repair damage), personnel occupational health and safety, as well as environmental emissions (e.g., process instability often result in higher than normal atmospheric emissions).

Notwithstanding the importance of Søderberg electrode design and management to ensure responsible, safe, and profitable smelting operations, very little research focussing specifically on Søderberg electrode related aspects have been published in the journal peer reviewed public domain. For instance, as far as the authors could assess (using the "Scopus" scientific search engines with the key words "Soderberg electrode"), only 5 such papers have been published in the last decade (i.e., 2011 to 2020) [4,11–14]. Several conference proceeding papers have also been published during this time, e.g., [2,3,5,15]. These conference proceeding papers also gave valuable topic specific insights. However, many such contributions were made principally to demonstrate the capability of commercial companies to serve their clients instead of divulging all relevant information as is common in academic journal papers.

The main aim of this work was to characterise a largely intact Søderberg electrode, removed from a ferrochrome SAF during a shutdown to rebuild many of the furnace components. The operational history for a month prior to the shutdown, procedures followed to sample the electrode and experimentally determined characteristics (e.g., electrical resistivity, degree of graphitisation, bulk density, porosity, and compressive breaking strength) are presented. As far as the authors could assess, such a characterisation of a real-world Søderberg electrode have not yet been presented in the peer reviewed public domain. Such data will contribute towards a better understanding of electrode management by operational personnel and assist researchers in identifying unresolved questions. Additionally, the characterisation data can be used to verify such characteristics in Søderberg electrode models, which have up to now mainly been restricted to temperature, current densities, and thermal stress profiles, e.g., [2,3,5,6].

2. Materials and Methods

2.1. Søderberg Electrode Sampling

On 31 July 2013, an operational ferrochrome SAF with 1.4 m casing outer diameter Søderberg electrodes was switched off, after following the appropriate preparations for a furnace rebuild. The furnace was allowed to cool down for 5 days. Thereafter, the number 2 electrode (Figure 1a indicating the numbering from a top view), was cut off with a diamond wire saw approximately 0.5 m below the contact shoes, as indicated in Figure 1b. The electrode stump was removed from the furnace with appropriate rigging equipment. Then, 100 mm outer diameter core drill samples were collected, with the 100 mm sample centred at 0.70, 1.15, 1.64, 2.16, and 2.70 m below the contact shoes. This core drilling was done through the entire diameter of the electrode, from the outside towards the delta side of the electrode. Here the term "delta" refers to the side of the electrode facing the centre of the SAF (see Figure 1a). An example of such a core drilled sample is presented in Figure 1c. The 100 mm diameter core samples were then cut into 10 mm disks (examples indicated in Figure 1d) with a commercial cut off grinder that was modified for the purpose. Precise lathe turned; tight fitting bushings were installed in the pivot point of this cut-off grinder to ensure accurate cutting. Additionally, it was permanently fitted on a table with specially designed cradles to hold the 100 mm tube-like core drilled electrode sample perpendicular to the blade of the cut-off grinder. Cylindrical sample pellets with outer diameters of 8 mm were then drilled out from these 10 mm thick disks with an appropriate diamond coated core drill fitted in a bench drill, as indicated in Figure 1e,f. The condition of a specific 100 mm thick disk determined how many such 8 mm $\times$ 10 mm cylindrical sample pellets could be obtained from it, with $\geq$10 being the norm. These 8 mm $\times$ 10 mm cylindrical sample pellets were used in all electrode characterisation experiments, unless stated otherwise. Since many of the characterisation techniques involved destructive analysis, the investigated characteristics were not performed on material sampled from the same positions within the case study electrode. Therefore, it was not possible to directly correlate (via correlation graphs) characteristics with one another.

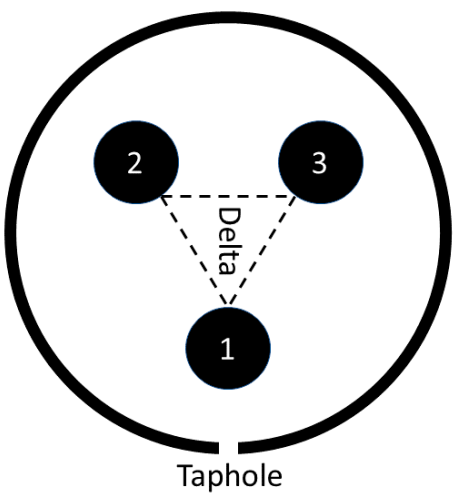

(**a**)

(**b**)

(**c**)

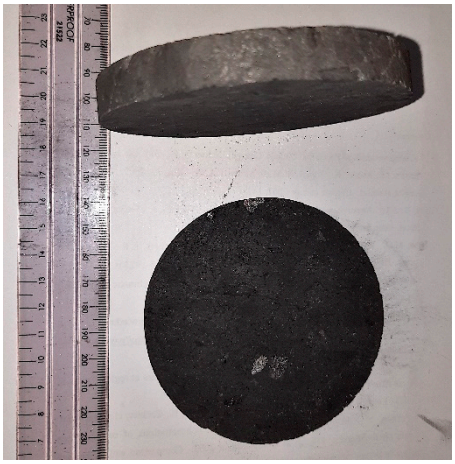

(**d**)

(**e**)

(**f**)

Figure 1. (**a**) Diagram from a top view indicating the electrode numbering of the SAF from which the electrode was removed; (**b**) photo indicating how the electrode was cut off, approximately 0.5 m below the contact shoes with a diamond wire saw; (**c**) an example 100 mm outer diameter core drill sample, collected by core drilling through the entire diameter of the electrode, from the outside towards the delta side of the electrode; (**d**) examples of 10 mm thick disks that were cut from the 100 mm diameter core samples; (**e**) example 10 mm thick disk, after 8 mm outer diameter cylindrical sample pellets were drilled out; (**f**) example 8 mm × 10 mm cylindrical sample pellets that were used in most experiments.

2.2. Electrical Resistivity Measurements

The electrical resistivities of cylindrical sample pellets were measured at room temperature using a GW Instek resistance precision meter (Model LCR-6020 Series). The meter can be used to measure inductance (L), capacitance (C), and resistance (R) of samples over a wide frequency (10 Hz–20 kHz), resistance (0.99–99.9 MΩ), and voltage range (10.00 mV–2.00 V). As indicated in Figure 2a, a two-probe device was manufactured (by the North-West University Instrument Makers) similar to the design presented by Heikkilä et al. [16] and connected to the LCR meter. This two-probe device had a bottom and a top probe, which were both turned from solid copper. The stainless steel tightening wheel mechanism (Figure 2a) was used to gently tighten a cylindrical sample pellet in-between these copper probes prior to a measurement. A torque wrench was then used to fasten the hex/Allen key located on top of the stainless steel tightening wheel mechanism further. This ensured that each sample was set under the same torque pressure (i.e., 0.5 Nm). The crocodile clamps of the LCR meter were clamped into fit-for-purpose holes drilled in the copper probes. These holes ensured consistent placement of the clamps on the probes, as well as consistent contact area between the clamps and the probes. The frame and connectors that attached the probes to the frame were made of polyvinyl chloride (PVC) plastic, to isolate the frame from the sample. As illustrated in Figure 2b, the face of the bottom copper probe on which the cylindrical sample pellet sat had a small rim on the outside, while the corresponding face of the top copper probe was flat. These shapes were used to ensure that the cylindrical sample pellets were held in-between the two copper probes in a repeatable manner. Both copper probes were also set on a 360° articulating spring mechanism. This kept the ends of the cylindrical sample pellet perpendicular to the probe faces, even if the cylindrical sample pellet ends were not perfectly perpendicular to the cylindrical sample pellet sides.

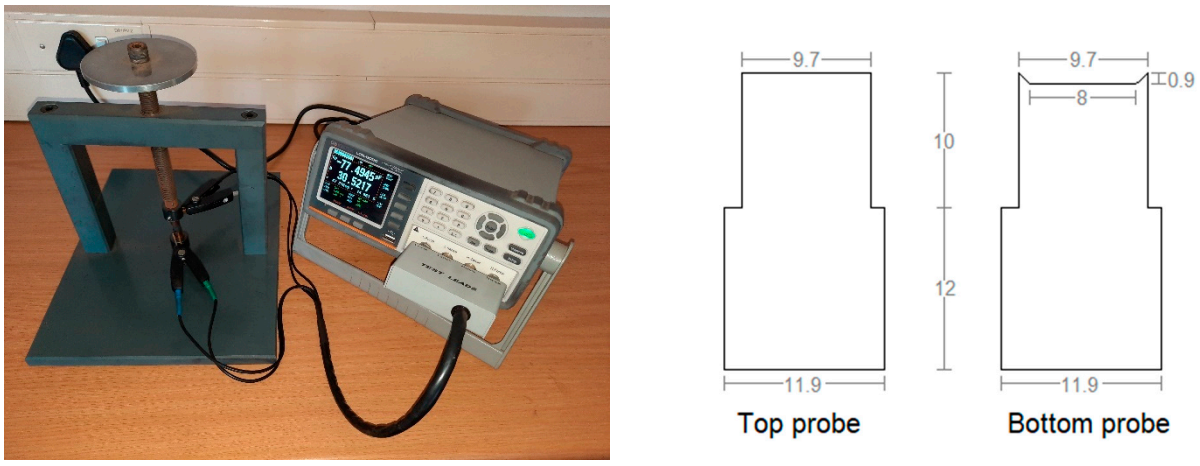

(**a**) (**b**)

Figure 2. (**a**) Photo indicating the GW Instek resistance precision meter (Model LCR-6020 Series) and two-probe device, similar to the design presented by Heikkilä et al. [16], used to measure electrical resistivity of the cylindrical sample pellets; (**b**) illustration indicating the shapes of the copper probes, in-between which the cylindrical sample pellets were held.

To ensure precision and accuracy, the LCR meter was switched on for 30 min and a daily calibration was conducted before measurements commenced. Cylindrical copper, aluminium, and stainless steel samples, which had dimensions similar to the cylindrical sample pellets, were measured during calibration. The calibration values were stored by the LCR meter to correct for errors caused by impedance of the experimental setup. The resistance values of the measured cylindrical sample pellets were calculated from Ohm's law:

$$R = V/I, \quad (1)$$

where R is the resistance (Ω), V is the voltage across the sample (V), and I is the measured current (A). Assuming uniform current distribution, the resistivity was calculated by Equation (2):

$$\rho = (V.A)/(I.H), \quad (2)$$

where ρ is the material resistivity (Ω·m), V is the voltage across the sample, I is the measured current (A), A is the cross-sectional area of the cylindrical sample (m^2), and H is the height of the sample (m).

2.3. Degree of Graphitisation Determinations

The degree of graphitisation (DOG) was determined with the so-called interlayer spacing or d_{002} method, based on X-Ray Diffraction (XRD) analysis [17]. This method is one of at least three recognised methods to determine DOG [18]. The powder generated during drilling of the 8 mm × 10 mm cylindrical sample pellets (as explained in Section 2.1) were used for this purpose. A small amount of silicon metal powder, used as a reference material, was added to the powdered Søderberg electrode material and mixed thoroughly, prior to analysis. The prepared samples were analysed on a Bruker D8 A25 DaVinci X-ray Diffractometer and LynxEye™ SuperSpeed Detector with xyz-stage mounted and using Cu-K radiation. The DOG was calculated with Equation (3) [17]:

$$DOG = (3.440 - d_{002})/(3.440 - 3.354) = (3.440 - d_{002})/0.086, \quad (3)$$

where DOG is the degree of graphitisation (unitless, with 1 indicating fully graphitised and 0 fully un-graphitised), 3.440 is the interlayer spacing of fully un-graphitised carbon (nm), 3.345 is the interlayer distance for pure graphite (nm), and d_{002} is the interlayer spacing derived from XRD analysis (nm).

2.4. Bulk Density Measurements

Bulk densities were measured using the ASTM C20-00 method [19]. Cylindrical sample pellets with 18 mm × 10 mm dimensions, obtained in a similar manner as the 8 mm × 10 mm cylindrical sample pellets (described in Section 2.1), were used in these determinations. The samples were first air dried at 105 °C for 3 h in an oven. After cooling in a desiccator, the samples were weighted (D). They were then saturated by boiling them in distilled water for 2 h. Thereafter, the samples were weighted in water to get the saturated weight (S). The bulk density was calculated with the following formula:

$$\rho = [D/(D - S)(\rho o - \rho L)] + \rho L, \quad (4)$$

where ρ is the bulk density of the sample ($g \cdot cm^{-3}$), D the sample weight after drying, S the saturated sample weight, ρo the density of water (taken as 0.9982 $g \cdot cm^{-3}$), and ρL the density of air (taken as 0.0012 $g \cdot cm^{-3}$).

Bulk densities were also measured with an AccyPyc II 1340 gas pycnometer. Søderberg electrode pieces remaining after the 8 mm × 10 mm cylindrical sample pellets were drilled out of the 10 mm thick disk (Figure 1e) were used for this purpose. Each sample was first weighed and then placed in a 35 cm^3 sample holder in the instrument chamber. The chamber was purged 5 times with 99.99% helium. A known quantity of gas at a known pressure was then expanded into the chamber and the new pressure measured. The difference between the initial and final pressures and the known volume of the chamber is then used (with the gas law) to calculate the volume of the sample. And with the sample mass, the sample bulk density could be calculated.

2.5. Porosity Determinations

Computerized tomography (CT) scanning was used to generate sample image slices, which could be processed to determine porosity. A Nikon XT H 225 ST with a 225 kV reflection target source and a Perkin Elmer 1620 detector CT instrument was used. Similar to the bulk density determinations (described in Section 2.4), Søderberg electrode pieces remain-

ing after the 8 mm × 10 mm cylindrical sample pellets were drilled out of the 10 mm thick disk (Figure 1e) were used. The samples were placed in glass poly tops stacked 6 high and wrapped in cellophane to keep them aligned and easy to handle. Each poly top was scanned individually, with 2000 sample image slices being generated per poly top. From these 2000 image slices per sample, 10 images which were evenly spaced (every 160 images between images 200 and 1800) were used for the actual porosity determinations. An example of a CT image slice is presented in Figure 3a. ImageJ (https://imagej.nih.gov/ij/, accessed 20/10/2020) was used to analyse the CT image slices. This was done by adjusting the threshold value so that the pores and background was red in colour (Figure 3b) in all images. In each image, the boundaries of the solid particle(s) visible in the CT image slice were then manually marked (indicated by the yellow line and white markers in Figure 3b). Thereafter, the measurement tool of ImageJ was used to determine the surface area of red pixels within the selected area(s), as a percentage of all the pixels within the selected area(s). This corresponded to the percentage pores in the particular CT image slice.

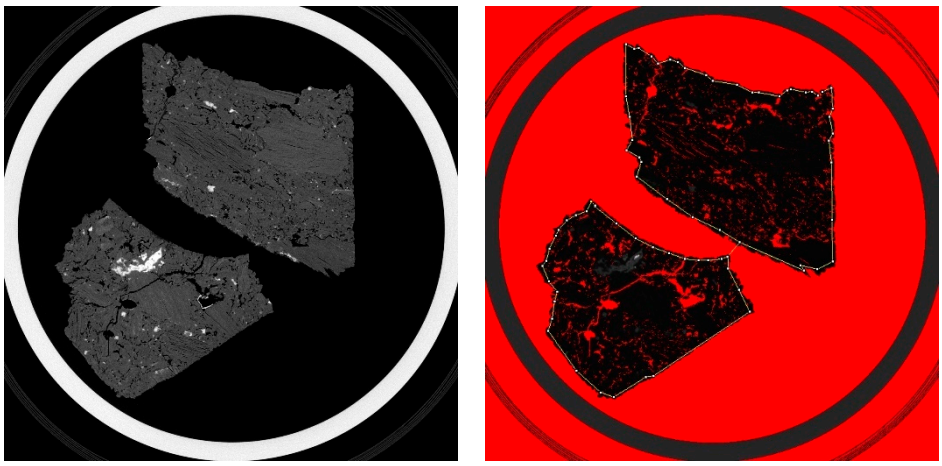

(**a**) (**b**)

Figure 3. (**a**) An example of a CT image slice; (**b**) ImageJ (https://imagej.nih.gov/ij/, accessed 20/10/2020) was used to analyse the CT image slices. The threshold value was adjusted so that the pores and background was red in colour. The boundaries of the solid particle(s) visible in the CT image slice were manually marked (indicated by the yellow line and white markers).

2.6. Compressive Breaking Strength Measurements

The compressive breaking strengths of 8 mm × 10 mm cylindrical sample pellets were determined using an Ametek Lloyd Instruments LRXplus 5 kN strength tester. NEXYGEN-Plus material test and data analysis software was used to control the instrument and capture the generated data. The speed of the compression plates moving towards one another was kept constant at 10 mm·min^{-1} during all compressive strength tests. The 8 mm × 10 mm cylindrical sample pellets were placed upright in the breaking strength machine (flat sample faces on compression plates), and the maximum load to induce breakage of each sample pellet was recorded.

2.7. Statistical Handling of Data

For electrical resistivity, between 10 and 30 of the 8 mm × 10 mm cylindrical sample pellets from a single 10 mm thick sample disk was measured, and each such pellet was measured 15 times. DOG determinations were only done once on each sample considered. In the ASTM C20-00 density experiments, 2 of the 18 mm × 10 mm sample pellets from a single 10 mm thick sample disk were considered, and each such pellet was used only once. In the gas pycnometry analyses, cuts off of sample pellets were used, and each analysis was repeated 5 times. Porosities based on CT scanning and image processing was conducted

as indicated in Section 2.6. For compressing breaking strength, between 10 and 30 of the 8 mm × 10 mm cylindrical sample pellets were tested from each considered 10 mm thick sample disk.

Where multiple repetitions were done, outliers were identified with a commonly applied method (e.g., https://www.mathworks.com/help/stats/box-plots.html, accessed 30/10/2020). This was done by multiplying the interquartile range (IQR) with 1.5, and datapoints that were above the 75th quartile plus the IQR and below the 25th percentile minus the IQR were disregarded in further calculations. Where applicable, standard deviations were presented with average values to indicate data repeatability.

3. Results and Discussion

3.1. Operational History

The results presented in this paper will only be relevant to Søderberg electrode use in SAF operations, if the case study electrode represented normal/stable operation. To explore this, total daily slipping taken on the electrode, daily average current passing through it, as well as daily average solid and liquid paste levels in the month prior to the furnace shutdown, are presented in Figure 4. From this data, it is evident that the slipping was relatively consistent (varied between 14 to 32 mm per day). No long slips (usually defined as >100 mm) were taken on this electrode, which indicates that the operational personnel considered its length as normal and that no breaks occurred during this 1 month period. The daily average current passing through the electrode varied between approximately 63 and 76 kA, and had an average of 72.2 kA in the period between 1 and 28 July 2013. This again indicates that no major operational issues occurred. In the last three days prior to the shutdown (29 to 31 July 2013) the energy input was purposefully reduced, which resulted in the average current passing through the electrode on the last operational day being 58.0 kA. Such a gradual reduction in power input contributes significantly to prevent thermal shock on the electrode [5]. Average daily solid (varying between 6.7 and 9.3 m) and liquid (varying 2.9 and 4.1 m) paste levels were normal, again with no indication that paste consumption increased or decreased significantly during the last month of operation. Considering all the afore-mentioned, in conjunction with visual inspection of the electrode and its length before being cut off (it was approximately 3 m long), it can be concluded that this case study electrode was representative of stable SAF operation.

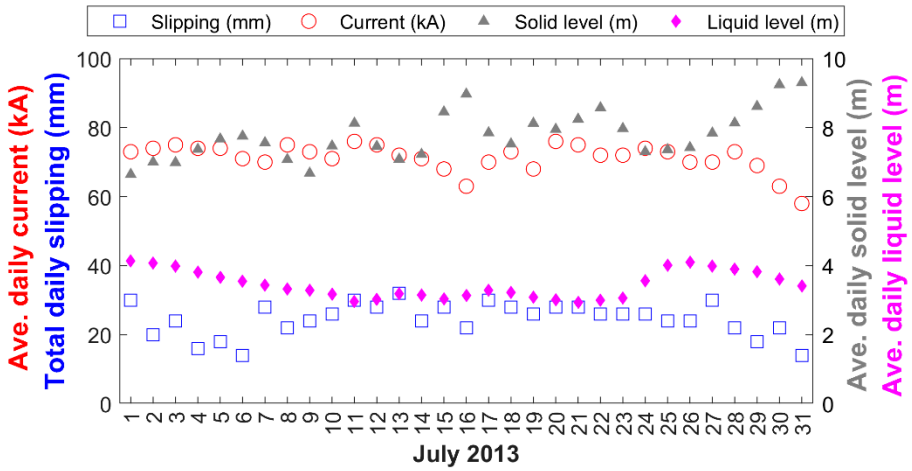

Figure 4. Total daily slipping taken on the case study electrode, daily average current passing through it, as well as daily average solid and liquid paste levels in the month prior to the furnace shutdown.

3.2. Electrical Resisitivity

The main function of Søderberg electrodes is to conduct electrical current into the smelting zone of the furnace. It is therefore fitting that electrical resistivity is the first

characteristic that is considered. Figure 5a presents the average measured resistivity and linear fitting of this data, as a function of length below the contact shoes and distance from the delta side of the electrode. It should be noted that no experimental data could be collected on, or very close to 0 and 1.4 m from the electrode delta side, since the 100 mm core drilled samples (Figure 1c) were typically $\leq$1.3 m long. This smaller electrode diameter than the original outer casing diameter of 1.4 m (introduced in Section 2.1), is due to several factors. Firstly, the mild steel casing usually burns off and/or melts within the first approximately 0.5 m below the contact shoes, which is also shown in Figure 1b for the specific electrode considered here. The casings used on the case study electrode was 3 mm thick. Therefore, 6 mm (3 mm on each side) can be attributed to the casing loss. Secondly, the electrode paste will shrink at temperatures above the baking isotherm [5]. This occurs since the carbonaceous material structure becomes more organised and closer to that of graphite, due to the increased temperature the electrode experiences as it descends. Thirdly, chemical corrosion, i.e., oxidation of the electrode carbon above the bed material, can also contribute, especially since the furnace considered here was an open-SAF. In open-SAFs, atmospheric air containing oxygen can relatively freely enter (determined by off-gas flow rate) and results in a partially oxidising environment above the bed material [20]. Lastly, physical erosion, due to frictional and mechanical forces exerted on the electrode, can also erode its outer perimeter. Due to all the afore-mentioned reasons, all result figures wherein the case study electrode diameter is specified will indicate it as 1.3, not 1.4 m.

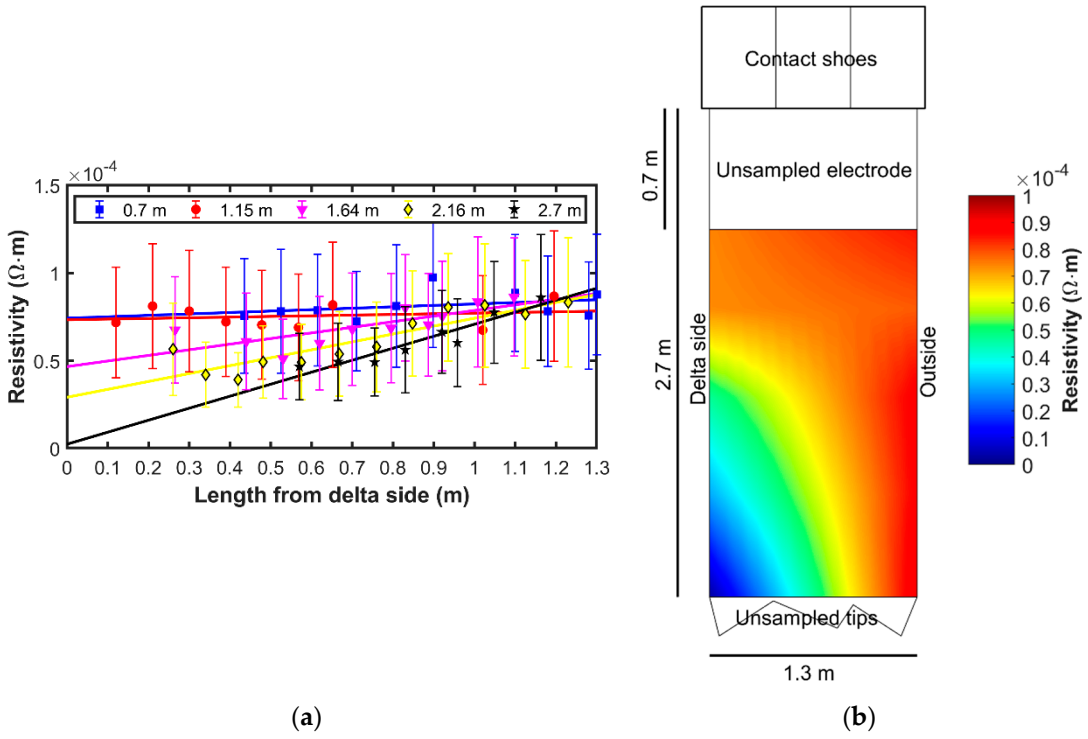

(**a**) (**b**)

Figure 5. (**a**) Average measured electrical resistivity (markers) and linear fitting of this data (lines), as a function of length below the contact shoes and distance from the delta side of the electrode; (**b**) 3D rendering of the fitted line data associated with resistivities at 10 mm intervals across the electrode at each of the lengths below the contacts shoes indicated in Figure 5a.

The standard deviations of the resistivity measurements presented in Figure 5a were relatively large. This was mostly due to the actual resistivities being so low (i.e., 10^{-5} to 10^{-6} Ω·m). Therefore, to ensure that the average values could be used to identify trends, very large numbers of measurements (i.e., N = 150 to 450) were conducted. Considering the average values, Figure 5a clearly indicates that the electrical resistivity on the outside (non-delta side) of the electrode between 0.7 and 2.7 m below the contact shoes, were essentially consistent. In contrast, the resistivity decreased (implying increased conductivity)

significantly from 0.7 to 2.7 m below the contact shoes on the delta side of the electrode. To visualise the electrical resistivity results better, the average data associated with the fitted lines presented in Figure 5a at 10 mm intervals across the diameter of the electrode at each of the investigated lengths below the contacts shoes were spatial interpolated across the entire investigated area (0.7 to 2.7 m below the contacts shoes), as indicated in Figure 5b. This was done using the "grid data" function in Matlab, with triangulation-based linear interpolation. In effect, this representation gives a 3-dimensional (3D) cross section perspective of the investigated electrode, excluding the unsampled electrode area directly below the contact shoes and the uneven electrode tips, with colour indicating the 3rd dimension. This 3D perspective indicates that resistivity was at its lowest at the bottom end on the delta side of the electrode, where the submerged arc would most likely jump off the electrode.

To contextualise the resistivity results presented in Figure 5a,b, they were firstly compared to high temperature bulk bed electrical resistivity values reported relatively recently for carbonaceous reductants (i.e., metallurgical coke, semi-coke, coal, and charcoal used in SAF smelting) [21]. Such high temperature bulk bed resistivities simulate the so-called coke bed (area around and below electrode tips in a SAF), where reductants serve as one of the primary electrical conductors [22]. At 1600 °C, it was found that the reductant bulk bed resistivities ranged from approximately 2×10^{-2} to 5×10^{-3} Ω·m [21]. These values were approximately 60 to 250 times higher (thus less conductive) than the approximate 8.40×10^{-5} Ω·m resistivity observed from 0.7 to 2.7 m below the contact shoes on the non-delta side of the electrode (reddish area on the right-hand side of Figure 5b). Correspondingly, the high temperature reductant bulk bed resistivities were approximately 2000 to 8000 times higher than the 2.4×10^{-6} Ω·m obtained at 2.7 m below the contact shoes on the electrode delta side (dark blue area in bottom left-hand corner of Figure 5b). Obviously, interparticle contact in a carbonaceous reductant bed is far inferior to the relatively solid carbonaceous mass of a Søderberg electrode, but the afore-mentioned comparison does indicate on a relative scale the conductivity ability of a Søderberg electrode.

To further contextualize the resistivity data presented in Figure 5a,b, it was compared to Søderberg electrode paste resistivity values derived from finite element thermoelectrical modelling [9,23]. These studies postulated resistivities to be 5.88×10^{-6} and 2.63×10^{-6} Ω·m in the electrode where the temperatures were 1000 and 2600 °C, respectively. Such temperatures correspond roughly to the 0.7 m (both delta and non-delta side) and 2.7 m (delta side only) positions below the contact shoes in Figure 5b, where resistivities were approximately 8.48×10^{-5} and 2.41×10^{-6} Ω·m, respectively. Although the modelled values [9,23] and values presented in the current work are in the same order, the differences in the corresponding values ($5.88 \times 10^{-6} - 2.63 \times 10^{-6} = 3.25 \times 10^{-6}$ Ω·m versus $8.48 \times 10^{-5} - 2.41 \times 10^{-6} = 8.24 \times 10^{-5}$ Ω·m) suggest that the models do not quickly enough account for lower resistivities as a function of electrode length below the contact shoes. Compared to the afore-mentioned models [9,23], a more comprehensive Søderberg electrode model has also previously been introduced [5]. This model might contain more detailed Søderberg electrode paste properties and might better account for the variation of such properties as a function of electrode length below the contact shoes. However, this model was essentially introduced as a black box to demonstrate the capabilities of a commercial company [5]; therefore, it was impossible to include the material properties specified therein in the current comparison. Furthermore, no evidence could be found that either of the three models [5,9,23] accounted for the very apparent asymmetrical variation of resistivities observed in the case study electrode (Figure 5b).

3.3. Degree of Graphitisation (DOG)

Figure 6a presents the average measured DOG and linear fitting of this data, as a function of length below the contact shoes and distance from the delta side of the electrode. Figure 6b presents the associated spatially interpolated 3D image. From both these figures (but particularly from Figure 6b) that visually represent the entire electrode cross section, it is evident that DOG is inversely related to the electrode resistivity (Figure 5b). This makes

sense, since increased DOG of the electrode paste will result in lower resistivity (i.e., higher conductivity). It is particularly insightful to also note that only the electrode tip on the delta side of the electrode (red area in bottom left-hand corner of Figure 6b, which corresponded to a maximum DOG of approximately 0.84), approached full graphitisation. As previously stated (Section 2.3), DOG is unitless, with 1 indicating fully graphitised and 0 fully ungraphitised. The majority of the investigated cross-sectional electrode area had DOG $\leq$ 0.5. As far as the authors could assess, DOG for a real world or a modelled Søderberg electrode has not yet been presented in the peer reviewed public domain; therefore, it was not possible to contextualise the measured DOG with such data.

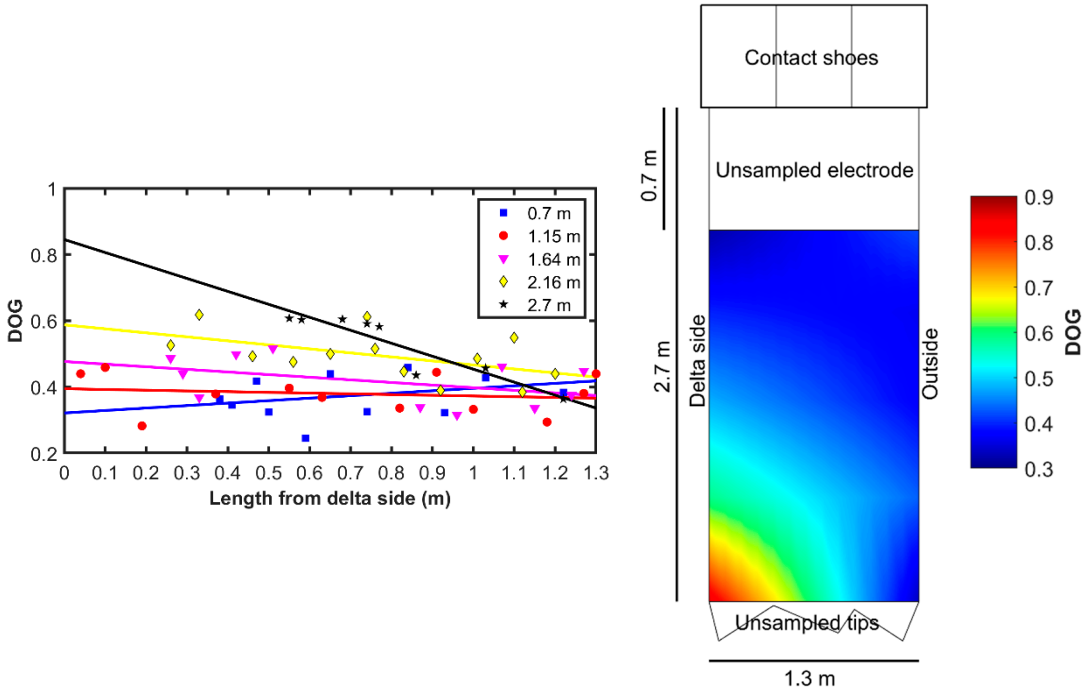

Figure 6. (**a**) Average measured degree of graphitisation (DOG) (markers) and linear fitting of this data (lines), as a function of length below the contact shoes and distance from the delta side of the electrode; (**b**) 3D rendering of the fitted line data associated with DOG at 10 mm intervals across the electrode at each of the lengths below the contacts shoes indicated in Figure 6a.

As indicated in the previous paragraph, to a large extent DOG determines the electrical resistivity of the Søderberg electrode. However, the DOG of the electrode paste is also related to other important characteristics. For instance, DOG is associated to possibly the most important aspect that cause electrode breaks, i.e., thermal stress. Particularly, green breaks (implying exposure of liquid paste in the break zone) in the contact shoes area are feared by operational personnel, due to the devastating consequences such breaks could have. In the most authoritative work on Søderberg electrode thermal stress, it is stated that some internal stresses are established during the process of electrode paste shrinkage below the contact shoes area, where the paste is baked at temperatures in excess of the basking isotherm temperature [5]. However, as previously stated, Søderberg electrode paste consists of a binder and a solid aggregate. In this case, the solid aggregate was calcined anthracite of various size factions, mixed to obtain the optimum composition. Although more environmentally friendly binders have been proposed than coal tar pitch, e.g., [24], it remains the most commonly used binder for Søderberg electrode pastes and was also used in the paste consumed by the case study electrode. In previous studies, it was proven that anthracite calcined at 1400 °C expands less than 1% and coal tar pitches prebaked at the maximum baking isotherm temperature (i.e., 475 °C, [11]) shrink approximately

12% if heated in a non-oxidising environment up to 1300 °C [4]. These opposing thermal expansion characteristics likely cause the thermal stresses below the contact shoes area referred to by Larsen et al. [5]. In contrast to calcined anthracite, uncalcined anthracite shrink 6 to 8% over the same temperature range. The significant difference between calcined and uncalcined anthracite clearly indicates how important the calcination process is to avoid additional thermal stresses forming just below the contact shoes area. Industrial calcination of anthracite to be used in electrode paste typically occur at temperatures above 1400 °C (as tested by Beukes et al. [4]); therefore, DOG similar to the blue area in Figure 6b (corresponding to DOG $\leq$ 0.5) is imparted on the electrode paste solid aggregate even before it is mixed into the electrode paste. The authors were not privileged to know the exact mixing ratio of the binder and aggregate used in the case study electrode. But, typically the mixture is dominated by aggregate, with the binder fractional contribution limited to just enable solid aggregate interparticle contact and proper paste flow characteristics above the softening point (to fill the casing in the area above the baking isotherm temperature).

3.4. Bulk Density

Figure 7a presents the average measured bulk density determined with ASTM C20-00 [19] (Section 2.4, 1st paragraph) as a function of length below the contact shoes and distance from the delta side of the electrode. Since ASTM C20-00 involves aqueous saturation of the samples via boiling, repeat analyses were not attempted. The density differences were relatively small (Figure 7a), therefore, even slight modification of the original characteristics that might occur during analysis or re-drying of the samples in preparation for reanalyses could make such reanalyses results misleading. Additionally, larger cylindrical sample pellets were used in this specific method (Section 2.4, 1st paragraph), which implied that significant additional sample material would have been required for reanalyses. This was not feasible, since a finite amount of material was available after sampling (Section 2.1). As is evident from the ASTM C20-00 results (Figure 7a), bulk densities did not indicate significant differences as a function of length below the contact shoes. Therefore, a single linear fitted line was drawn through all the data, which indicated a slight increase in densities toward the delta side of the electrode.

To verify that densities did not differ as a function of length below the contact shoes and to determine standard deviations, bulk densities were also determined with gas pycnometry (Section 2.4, 2nd paragraph). The gas pycnometry densities (Figure 7b), in contrast to the ASTM C20-00 results (Figure 7a), did indicate that bulk densities differed as a function of length below the contact shoes. This indicates that gas pycnometry is possibly a more precise method than ASTM C20-00, or alternatively that the difference in atom/molecule size (i.e., He used in gas pycnometry vs. H_2O used ASTM C20-00) play a significant role in the measured results. To visualise these gas pycnometry results, Figure 7c presents the associated spatially interpolated 3D image, based on the fitted data presented in Figure 7b. Considering the very similar perspectives indicated by the bulk densities presented here (Figure 7c) and the DOG presented earlier (Figure 6b), it is inferred that the increased bulk densities observed, particularly on the delta side of the electrode as a function of length below the contact shoes, were due to increased DOG. Increased DOG will result in further shrinkage of the carbonaceous Søderberg electrode paste material.

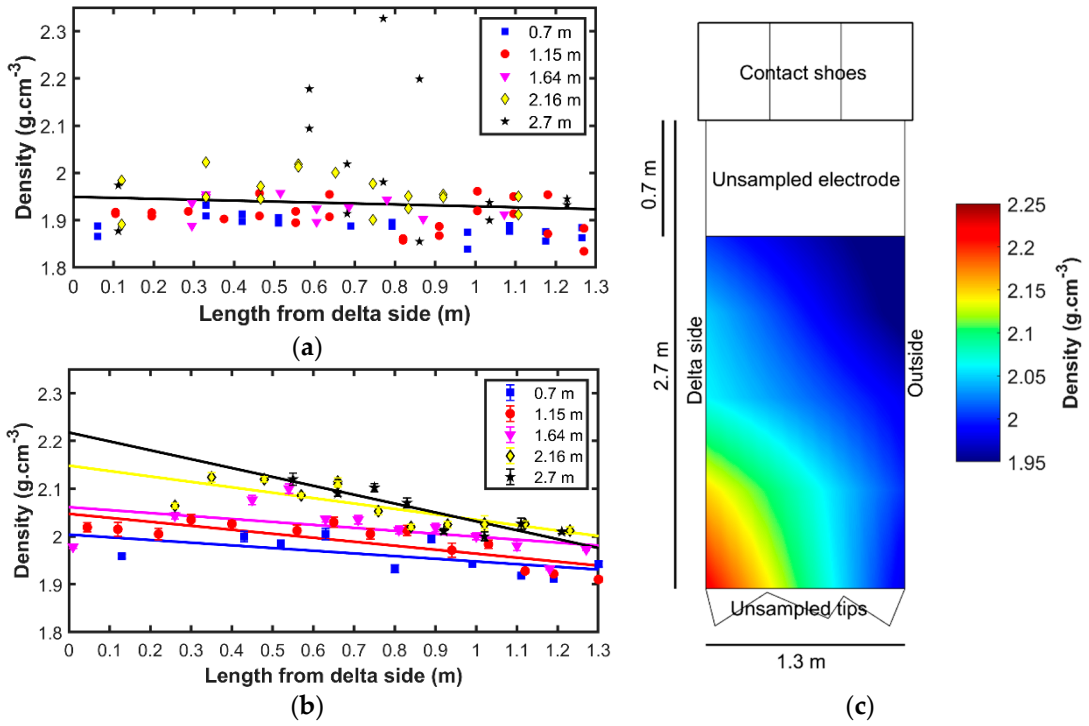

Figure 7. (**a**) ASTM C20-00 average measured bulk densities (markers) as a function of length below the contact shoes and distance from the delta side of the electrode. A single linear fitting of all this data (line) is also indicated; (**b**) gas pycnometry average measured bulk densities (markers) and linear fitting of this data (lines), as a function of length below the contact shoes and distance from the delta side of the electrode; (**c**) 3D rendering of the fitted line data associated with bulk densities at 10 mm intervals across the electrode at each of the lengths below the contacts shoes indicated in Figure 7b.

3.5. Porosity

Figure 8a presents the average measured porosity. As is evident, no significant difference in porosity as a function of length below the contact shoes were observed. However, a slight increase in porosity was observed, near the electrode perimeter on both the delta and non-delta side. Therefore, a 2nd order polynomial (solid line in Figure 8a) fitted the data best. The corresponding spatially interpolated 3D image is presented in Figure 8b.

Since the industrial application of the Søderberg electrode started, it has been proven that volatiles released from the liquid paste just above the baking isotherm (indicated by black dotted line in Figure 9a) cannot rise if proper (high enough) liquid and solid paste levels are maintained e.g., [25]. Conversely, if "smoke" is observed at the top of the electrode column casing, it serves as a serious warning signal to operational personal that the liquid paste level of that electrode is critically low and/or that the liquid paste is too hot. Since the volatiles just above the baking isotherm cannot rise, they escape downward through the pores of the already baked electrode [25]. Cracking of these descending volatiles (due to the high temperature of the baked electrode) leaves a considerable amount of carbon in the pores of the baked electrode paste just below the contact shoes area, which improves its quality [25]. This process is illustrated by the purple arrows in the enlarged area of Figure 9a. The blue temperature isotherm in the enlarged area of Figure 9b represents a slightly hotter isotherm temperature than the baking isotherm. Considering this diagram, one would assume that the route of least resistance for volatiles to escape would be towards the outside of the electrode (i.e., shortest route of baked electrode paste), not the electrode core. Theoretically, this process would therefore slightly reduce the porosity of the electrode towards its perimeter, which is contrary to the experimental results presented (Figure 8a,b).

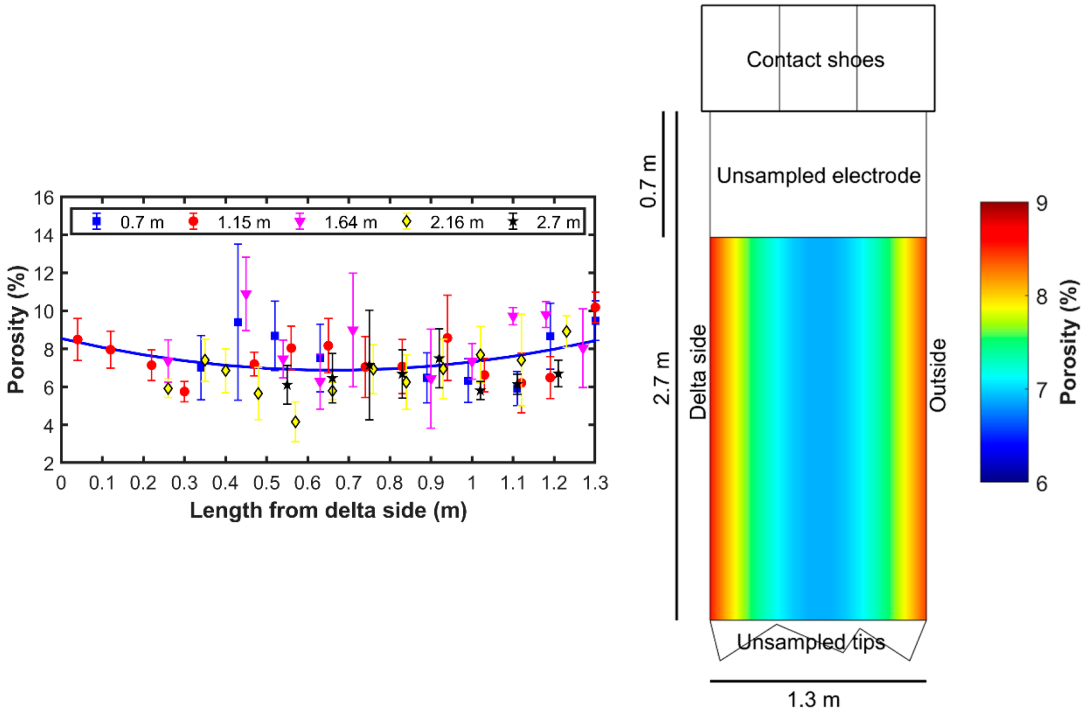

Figure 8. (**a**) Average measured porosity (markers), as a function of length below the contact shoes and distance from the delta side of the electrode, as well as a single 2nd order polynomial fit of this data (line); (**b**) 3D rendering of the fitted line data associated with porosities at 10 mm intervals across the electrode at each of the lengths below the contacts shoes indicated in Figure 8a.

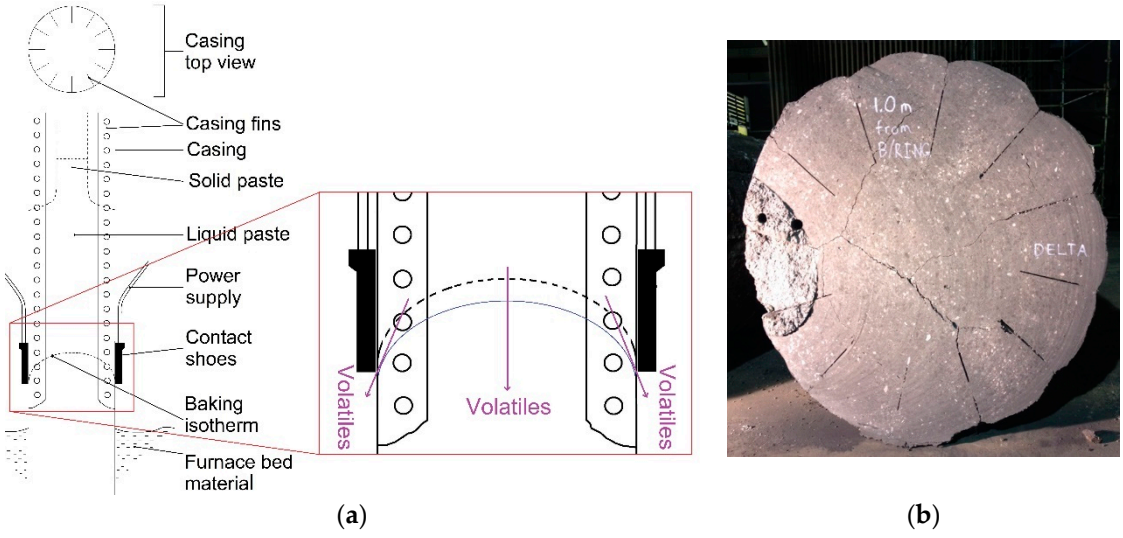

Figure 9. (**a**) Representation of a partial Søderberg electrode column, adapted from Beukes et al. [4], with the contact shoes area enlarged (indicated by the square red block); (**b**) cross section of another electrode from the same SAF that was cut off with a diamond wire saw approximately 1.0 m below the contact shoes.

There could be two other factors that counter the possible decrease in porosity towards the electrode perimeter, caused by descending volatile cracking. Firstly, liquid electrode paste segregation (i.e., partial separation of the pitch binder and solid aggregate), as illustrated by Nelson and Prins [8], could result in significant differences in the baked electrode properties considered diagonally across an electrode. However, calcined anthracite has

a much higher DOG than coal tar pitch baked above the maximum baking isotherm temperature (i.e., 475 °C, [11]). Therefore, if paste segregation caused the differences in observed porosities (Figure 8b), corresponding differences in DOG diagonally across the case study electrode would likely also have evident at the first level below the contact shoes investigated (i.e., 0.7 m). This was not the case (Figure 6b); therefore, paste segregation is unlikely to be the cause. Also, visual inspection of the sampled electrode did not indicate any segregation. The second possible contributing factor that could increase porosity of the case study electrode is chemical corrosion, i.e., oxidation of the electrode carbon above the bed material. As previously stated, this can especially occur in an open-SAF, as considered here [20]. Figure 9b shows the diagonal cross section of another electrode from the same SAF that was cut off approximately 1.0 m below the contacts shoes. As is evident from this electrode, corrosion on the outer perimeter was more significant in the areas where the casing fins occurred. This indicates that the gaps remaining after the casing burned off and/or melted away, formed paths for oxygen penetration, and associated oxidation of the carbon material. This describes the process on a macroscale, but it is postulated that the same process occurs on a pore size scale, which will increase pore volumes and hence porosity preferentially on the electrode perimeter.

3.6. Compressive Breaking Strength

Figure 10 presents the average measured compressive breaking strength as a function of length below the contact shoes and distance from the electrode delta side. As is evident, no significant difference was observed over the entire electrode area investigated. This indicates that compressive breaking strength was not related to DOG, as was the case for electrical resistivity and bulk density, nor was it influenced by physical and/or chemical processes, as postulated for the porosities.

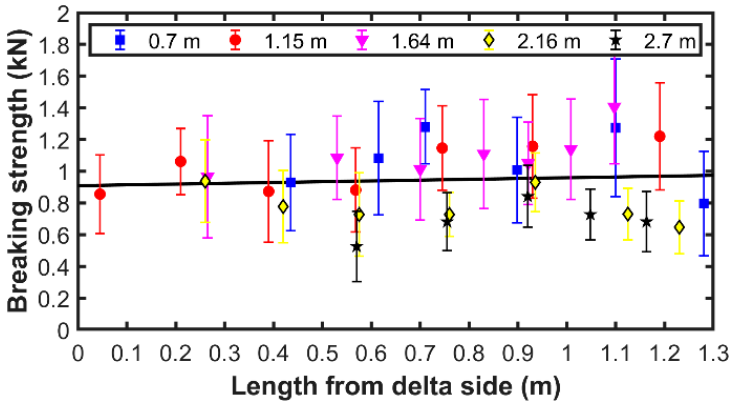

Figure 10. Average measured compressive breaking strength (markers), as a function of length below the contact shoes and distance from the delta side of the electrode, as well as a single linear fit of this data (line).

4. Conclusions

As far as the authors could assess, this work presents the first characterisation of a real-world Søderberg electrode, presented in a peer reviewed journal in the public domain. Obviously, a study such as this has limitations. For instance, measurements of the characteristics were conducted at room temperature, instead of at the operational temperatures. Also, the study was conducted on an electrode removed for an open-SAF producing ferrochrome, for which some characteristics might differ from Søderberg electrodes operating in other furnace types and smelting different materials. However, all these limitations are similar to furnace dig-out studies, e.g., [26–28], which have to a large degree formed our current understanding of zones within furnaces. Another data limitation of the current work was that the case study electrode did not include the area directly above, in, and just below the contact shoes. Understanding this area is critical.

Unfortunately, this section of the electrode could not be obtained, since that would have entailed starting up the furnace with a green electrode tip.

The results presented in this paper provided valuable insights, but also indicated questions/topics that need to be considered in future research. The operational data for the month prior to the furnace rebuild, during which the case study electrode was removed, proved that the electrode was a representative specimen. The characterisation results indicated no significant electrical resistivity, DOG, and bulk density changes from 0.7 to 2.7 m on the non-delta side of the electrode, while these characteristics changed relatively significantly on the delta side of the electrode. The area where the submerged arc would mostly like jump off the electrode clearly had the lowest resistivity, as well as highest DOG and bulk density. It is currently not evident from literature if these very asymmetrical characteristics can be accurately predicted by Søderberg electrode models, e.g., [5,9,23]. However, all such models predict temperature isotherms/curves. The temperature to which Søderberg electrode paste is exposed determines the DOG, to a large degree. As shown here, the DOG in turn determine to a large extent, the resistivities and bulk densities. Therefore, it would be advantageous if Søderberg electrode models could accurately replicate the DOG presented here. To aid such comparison, the resistivities, DOG, and bulk densities associated with the fitted lines at 10 mm intervals across the diameter of the electrode at each of the investigated lengths below the contacts shoes prior to being spatial interpolated to generate the 3D images are presented in Appendix A. For future experimental studies, it is recommended that the DOG of calcined anthracite and coal tar pitch be investigated separately (not as a mixture in electrode paste), in relation to electrical resistivity and bulk density, as well as other characteristics such as thermal expansion. This will enable better understanding of the individual contribution of these two components, to the combined results observed for electrode paste.

The determination of porosity with CT scanning combined with image processing is likely more accurate than conventional methods. However, the manual marking of the areas to be included in the calculations for porosity made the method time consuming and less attractive. Research has already been initiated to automate the determination of the particle rims within CT image slices and calculation of porosities and pore volumes. From the presented porosity data, no significant difference in porosities, as a function of length below the contact shoes, were evident. However, slight increases in porosities were observed near the electrode perimeter on both the delta and non-delta sides, which was fitted best with a 2nd order polynomial function. It was postulated that chemical corrosion, i.e., oxidation of the carbonaceous material, increases the pore volumes in the baked electrode paste near the perimeter.

The compressive breaking strength data revealed no significant trends. Therefore, operational personnel should not be concerned about breaking strength in the region well below the baking isotherm being during stable operation. As previously stated [5], thermal stresses that form in and just below the baking isotherm, as well as thermal stress differences between the perimeter and core of the electrode formed due to prolong furnace downtime, remain the most likely reasons for breaks of electrodes with no other apparent dysfunctionalities.

Considering the value of studies such as this, hopefully the current work will also encourage the donation of similar case study electrodes to researchers. As an example, the authors belatedly became aware of 2 separate 63 MVA closed-SAFs, for which the electrode outer casing diameters were increased from 1.5 to 1.6 m. In order to do so, 6 entire electrode columns, including the casings with un-melted solid paste at the top, down to the baked electrode tips at the bottom, were removed and discarded. However, no one in the research community was notified, nor did the company/operational personnel reach out to researchers. Such large scale, real-world samples are scarce; therefore, opportunities such as this should not be missed.

Author Contributions: Conceptualisation, J.P.B., P.G.v.Z., and D.D.; measurement methodology, J.P.B., R.I.G., M.T., E.R., and J.D.S.; experimental investigation, R.I.G. and M.M.; writing—original

draft preparation, J.P.B.; writing—review and editing, all co-authors; study supervision, J.P.B. and P.G.v.Z.; funding acquisition, J.P.B., P.G.v.Z., M.T., and E.R. All authors have read and agreed to the published version of the manuscript.

Funding: Funding for this project from SFI Metal Production (Centre for Research-based Innovation, 237738) and the Thanos project (INPART project 309475), both supported by the Research Council of Norway (RCN), is acknowledged, as well as industrial partners that support SFI Metal Production.

Acknowledgments: The authors thank the Wonderkop Smelter, which is part of Glencore Alloys, South Africa, for donating the Søderberg electrode considered in this study and supplying the operational data for the electrode.

Conflicts of Interest: The authors declare no conflict of interest. The work described is original research that has not been published previously, and is not under consideration for publication elsewhere, in whole or in part.

Appendix A

Table A1. The electrical resistivity, DOG, and bulk density data associated with the fitted lines in Figure 5a, Figure 6a, and Figure 7b, at 10 mm intervals across the diameter of the electrode at each of the investigated lengths below the contacts shoes, respectively. This data was spatially interpolated to generate the 3D images presented in Figure 5b, Figure 6b, and Figure 7c, respectively.

Distance from Delta Side (m)	Distance below the Contact Shoes (m)				
	0.70	**1.15**	**1.64**	**2.16**	**2.70**
	Resistivity (Ω·m)				
0	7.42×10^{-5}	7.34×10^{-5}	4.66×10^{-5}	2.92×10^{-5}	2.41×10^{-6}
0.1	7.51×10^{-5}	7.37×10^{-5}	4.98×10^{-5}	3.37×10^{-5}	9.25×10^{-6}
0.2	7.59×10^{-5}	7.41×10^{-5}	5.30×10^{-5}	3.82×10^{-5}	1.61×10^{-5}
0.3	7.67×10^{-5}	7.45×10^{-5}	5.62×10^{-5}	4.27×10^{-5}	2.29×10^{-5}
0.4	7.75×10^{-5}	7.49×10^{-5}	5.94×10^{-5}	4.72×10^{-5}	2.98×10^{-5}
0.5	7.83×10^{-5}	7.52×10^{-5}	6.26×10^{-5}	5.17×10^{-5}	3.66×10^{-5}
0.6	7.91×10^{-5}	7.56×10^{-5}	6.58×10^{-5}	5.62×10^{-5}	4.35×10^{-5}
0.7	7.99×10^{-5}	7.60×10^{-5}	6.91×10^{-5}	6.07×10^{-5}	5.03×10^{-5}
0.8	8.07×10^{-5}	7.64×10^{-5}	7.23×10^{-5}	6.52×10^{-5}	5.71×10^{-5}
0.9	8.15×10^{-5}	7.68×10^{-5}	7.55×10^{-5}	6.97×10^{-5}	6.40×10^{-5}
1.0	8.24×10^{-5}	7.71×10^{-5}	7.87×10^{-5}	7.42×10^{-5}	7.08×10^{-5}
1.1	8.32×10^{-5}	7.75×10^{-5}	8.19×10^{-5}	7.88×10^{-5}	7.77×10^{-5}
1.2	8.40×10^{-5}	7.79×10^{-5}	8.51×10^{-5}	8.33×10^{-5}	8.45×10^{-5}
1.3	8.48×10^{-5}	7.83×10^{-5}	8.83×10^{-5}	8.78×10^{-5}	9.13×10^{-5}
	DOG				
0	0.32	0.39	0.48	0.59	0.86
0.1	0.33	0.39	0.47	0.58	0.81
0.2	0.34	0.39	0.46	0.56	0.77
0.3	0.34	0.39	0.45	0.55	0.73
0.4	0.35	0.39	0.45	0.54	0.69
0.5	0.36	0.38	0.44	0.53	0.65
0.6	0.37	0.38	0.43	0.52	0.61
0.7	0.37	0.38	0.42	0.50	0.57
0.8	0.38	0.38	0.41	0.49	0.53
0.9	0.39	0.38	0.41	0.48	0.49
1.0	0.40	0.37	0.40	0.47	0.45
1.1	0.40	0.37	0.39	0.46	0.41
1.2	0.41	0.37	0.38	0.44	0.38
1.3	0.42	0.37	0.37	0.43	0.34

Table A1. *Cont.*

Distance from Delta Side (m)	Distance below the Contact Shoes (m)				
	0.70	**1.15**	**1.64**	**2.16**	**2.70**
	Bulk density (g·cm^{-3})				
0	2.00	2.05	2.06	2.15	2.22
0.1	1.99	2.04	2.06	2.14	2.20
0.2	1.99	2.03	2.05	2.13	2.18
0.3	1.99	2.02	2.04	2.11	2.16
0.4	1.98	2.01	2.04	2.10	2.14
0.5	1.98	2.01	2.03	2.10	2.12
0.6	1.97	2.00	2.02	2.08	2.11
0.7	1.96	1.99	2.01	2.07	2.09
0.8	1.96	1.98	2.01	2.06	2.07
0.9	1.95	1.97	2.00	2.05	2.05
1.0	1.95	1.96	2.00	2.04	2.03
1.1	1.94	1.96	1.99	2.02	2.01
1.2	1.94	1.95	1.99	2.01	2.00
1.3	1.93	1.94	1.98	2.00	1.98

References

1. Richards, J.W. The Söderberg self-Baking continuous electrode. In Proceedings of the Thirty-Seventh General Meeting of the American Electrochemical Society, Boston, MA, USA, 8 April 1920; pp. 169–188.
2. Larsen, B. Electrode models for Søderberg electrodes. In Proceedings of the Fifth Platinum Conference, Sun City, South Africa, 18 September 2012; pp. 275–286.
3. Skjeldestad, A.; Tangstad, M.; Lindstad, L.; Larsen, B. Temperature profiles in Søderberg electrodes. In Proceedings of the Fourteenth International Ferroalloys Congress (INFACON), Kiev, Ukraine, 31 May–4 June 2015; pp. 327–337.
4. Beukes, J.P.; Roos, H.; Shoko, L.; Van Zyl, P.G.; Neomagus, H.W.J.P.; Strydom, C.A.; Dawson, N.F. The use of thermomechanical analysis to characterise Söderberg electrode paste raw materials. *Miner. Eng.* **2013**, *46*, 167–176. [CrossRef]
5. Larsen, B.; Feldborg, H.; Halvorsen, S.A. Minimizing thermal stress during shutdown of Søderberg electrodes. In Proceedings of the Thirteenth International Ferroalloys Congress (INFACON), Almaty, Kazakhstan, 9–13 June 2013; pp. 453–466.
6. Meyjes, R.P.; Venter, J.; Van Rooyen, U. Advanced modelling and baking of electrodes. In Proceedings of the Twelfth International Ferroalloys Congress (INFACON), Helsinki, Finland, 6–9 June 2010; pp. 779–788.
7. Ray, C.R.; Sahoo, P.K.; Rao, S.S. Electrode management–investigation into soft breaks at 48MVA FeCr closed furnace. In Proceedings of the Eleventh International Ferroalloys Congress (INFACON), New Delhi, India, 18–21 February 2007; pp. 742–751.
8. Nelson, L.R.; Prins, F.X. Insights into the influences of paste addition and levels on Söderberg electrode management. In Proceedings of the Tenth International Ferroalloys Congress (INFACON), Cape Town, South Africa, 1–4 February 2004; pp. 418–431.
9. Mc Dougall, I.; Smith, C.F.R.; Olmstead, B.; Gericke, W.A. Finite element model of a Søderberg electrode with an application in casing design. In Proceedings of the Tenth International Ferroalloys Congress (INFACON), Cape Town, South Africa, 1–4 February 2004; pp. 575–584.
10. Larsen, B.; Amaro, J.P.M.; Nascimento, S.Z.; Fidje, K.; Gran, H. Melting and densification of electrode paste briquettes in Søderberg electrodes. In Proceedings of the Tenth International Ferroalloys Congress (INFACON), Cape Town, South Africa, 1–4 February 2004; pp. 405–417.
11. Shoko, L.; Beukes, J.P.; Strydom, C.A. Determining the baking isotherm temperature of Söderberg electrodes and associated structural changes. *Miner. Eng.* **2013**, *49*, 33–39. [CrossRef]
12. White, J.F.; Rigas, K.; Andersson, S.P.; Glaser, B. Thermal properties of Söderberg electrode materials. *Metall. Mater. Trans. B* **2020**, *51*, 1928–1932. [CrossRef]
13. Karalis, K.T.; Karkalos, N.; Cheimarios, N.; Antipas, G.S.E.; Xenidis, A.; Boudouvis, A.G. A CFD analysis of slag properties, electrode shape and immersion depth effects on electric submerged arc furnace heating in ferronickel processing. *Appl. Math. Model.* **2016**, *40*, 9052–9066. [CrossRef]
14. Shoko, L.; Beukes, J.P.; Strydom, C.A.; Larsen, B.; Lindstad, L. Predicting the toluene-And quinoline insoluble contents of coal tar pitches used as binders in Söderberg electrodes. *Int. J. Miner. Process.* **2015**, *144*, 46–49. [CrossRef]
15. Jordan, D.T.; Hockaday, C.J. Development of a camera-Based Söderberg electrode slip measurement device. In Proceedings of the Thirteenth International Ferroalloys Congress (INFACON), Almaty, Kazakhstan, 9–13 June 2013; pp. 417–426.
16. Heikkilä, A.M.; Pussinen, J.H.; Mattila, O.J.; Fabritius, T.M.J. About electrical properties of chromite pellets –Effect of reduction degree. *Steel Res. Int.* **2015**, *86*, 121–128. [CrossRef]

17. Zou, L.; Huang, B.; Huang, Y.; Huang, Q.; Wang, C. An investigation of heterogeneity of the degree of graphitization in carbon-carbon composites. *Mater. Chem. Phys.* **2003**, *82*, 654–662. [CrossRef]
18. Zhang, Z.; Wang, Q. The new method of XRD measurement of the degree of disorder for anode coke material. *Crystals* **2017**, *7*, 1–10. [CrossRef]
19. C20-00, ASTM. *Standard Test Method for Apparent Porosity, Water Absorption, Apparent Specific Gravity, and Bulk Density of Burned Refractory Brick and Shapes by Boiling Water*; ASTM International: West Conshohocken, PA, USA, 2010.
20. Beukes, J.P.; Du Preez, S.P.; Van Zyl, P.G.; Paktunc, D.; Fabritius, T.; Päätalo, M.; Cramer, M. Review of Cr(VI) environmental practices in the chromite mining and smelting industry–Relevance to development of the Ring of Fire, Canada. *J. Clean. Prod.* **2017**, *165*, 874–889. [CrossRef]
21. Surup, G.; Pedersen, T.; Chaldien, A.; Beukes, J.P.; Tangstad, M. Electrical resistivity of carbonaceous bed material at high temperature. *Processes* **2020**, *8*, 0933. [CrossRef]
22. Tangstad, M.; Beukes, J.P.; Steenkamp, J.; Ringdalen, E. Chapter 14. Coal-Based reducing agents in ferroalloys and silicon production. In *New Trends in Coal Conversion*; Suárez-Ruiz, I., Rubiera, F., Diez, M., Eds.; Elsevier: Duxford, UK, 2019; pp. 405–438. Available online: http://dx.doi.org/10.1016/B978-0-08-102201-6.00014-5 (accessed on 30 October 2020).
23. Bermúdez, A.; Bullón, J.; Pena, F. A finite element method for the thermoelectrical modelling of electrodes. *Commun. Numer. Methods Eng.* **1998**, *14*, 581–593. [CrossRef]
24. Ciesińska, W.; Zieliński, J.; Brzozowska, T. Thermal treatment of pitch-polymer blends. *J. Therm. Anal. Calorim.* **2009**, *95*, 193–196. [CrossRef]
25. Sem, M.O. The Söderberg self-baking electrode. *J. Electrochem. Soc.* **1954**, *101*, 487–492. [CrossRef]
26. Wedepohl, A.; Barcza, N.A. The "dig-Out" of a ferrochromium furnace. *Spec. Publ. Geol. Soc. S. Afr.* **1983**, *7*, 351–363.
27. Nell, J.; Joubert, C. Phase chemistry of digout samples from a ferrosilicon furnace. In Proceedings of the Thirteenth International Ferroalloys Congress (INFACON), Almaty, Kazakhstan, 9–13 June 2013; pp. 265–272.
28. Steenkamp, J.D.; Gous, J.P.; Grote, W.; Cromarty, R.; Gous, H.J. Process zones observed in a 48 MVA submerged arc furnace producing silicomanganese according to the ore-Based process. In Proceedings of the Extraction 2018, The Minerals, Metals & Materials Series, Ottawa, ON, Canada, 26–29 August 2018. Available online: https://doi.org/10.1007/978-3-319-95022-8_50 (accessed on 30 October 2020).